npj | climate and atmospheric science

www.nature.com/npjclimatsci

ARTICLE OPEN

Check for updates

Atmospheric aerosol size distribution impacts radiative effects over the Himalayas via modulating aerosol single-scattering albedo

Pengfei Tian[1], Zeren Yu[1], Chen Cui[1], Jianping Huang[1,2]✉, Chenliang Kang[1], Jinsen Shi[1,2], Xianjie Cao[1] and Lei Zhang[1,2]✉

The single-scattering albedo (SSA) of atmospheric aerosols is a key parameter that controls aerosol radiative effects. The variation of SSA is thought to be mainly regulated by aerosol absorption in the Himalayas and South Asia, but observations contradict this idea. In situ field campaigns conducted over two Himalayan sites revealed that SSA was strongly dependent on scattering but weakly correlated with absorption. Observational results combined with the Mie theory further illustrated that SSA was primarily modulated by size distribution rather than absorption. Aerosol Robotic Network (AERONET) data showed similar impacts of size distribution on SSA and that aerosol radiative forcing efficiencies were significantly dependent on SSA. Aerosol size distribution therefore considerably affects radiative forcing by modulating aerosol SSA over the Himalayas. This study highlighted the influence of aerosol size distribution on radiative forcing over the Himalayas, which has important implications for understanding aerosol radiative effects globally.

npj Climate and Atmospheric Science (2023)6:54 ; https://doi.org/10.1038/s41612-023-00368-5

INTRODUCTION

Light scattering and absorption of atmospheric aerosols have important radiative effects on the Earth−atmosphere system through aerosol−radiation and aerosol−cloud interactions[1–5]. The single-scattering albedo (SSA), defined as the ratio between aerosol scattering and extinction (scattering plus absorption) at a specific wavelength, is the most intensive parameter controlling aerosol radiative effects[6–8]. It determines not only the magnitude but also the sign of aerosol radiative forcing. For example, a slight change in SSA can lead to significant variation in radiative forcing, and SSA values lower than 0.85 may result in positive forcing at the top of the atmosphere (TOA)[9–11]. Studies have also revealed that SSA is a major contributor to radiative forcing uncertainties in climate models[12–14].

SSA is mainly governed by aerosol chemical compositions, size distribution, and mixing state[15–17]. The influence of chemical species, especially absorbing species, such as black carbon (BC), brown carbon (BrC), and mineral dust, on SSA has been widely studied[18–22]. Massive anthropogenic emissions caused high absorbing aerosol loading in South Asia, which resulted in very low ambient SSAs over urban sites in this region, including 0.68 at 525 nm over Delhi, India[23], 0.73 at 500 nm over Bangalore, India[24], and 0.76 at 500 nm in Kanpur, India[25]. The transport of high absorbing aerosols from South Asia has also been revealed to cause low SSA over a few sites in the Himalayas based on in situ observations, including 0.78 at Godavari (1600 m a.s.l)[26] and 0.83 at Mukteshwar (2180 m a.s.l)[27]. Studies have further revealed that aerosols age and become more absorbing with increasing altitude over the Himalayas[28,29]. Such low SSAs likely caused large radiative forcing in South Asia and the Himalayas[30–32].

However, more factors seemed to significantly affect SSA in addition to aerosol absorption in the Himalayas. Continuous surface observations showed that SSA values were related to the ratio between Aitken and accumulation-mode aerosol number concentrations over a Himalayan site[33], which indicated the possible influence of aerosol size distribution on SSA in the Himalayas. A comparative study based on model simulations and surface observations concluded that large-size absorbing particles (i.e., mineral dust) rather than BC primarily determined aerosol absorption and SSA[34]. Based on Aerosol Robotic Network (AERONET) columnar data, a recent study revealed that SSA decreased with increasing altitude over three sites in the Himalayan foothills[35], which was explained by the higher BC absorbing aerosol optical depth (AAOD) at higher altitudes. However, the fine volume fractions decreased while linear depolarization ratios increased with increasing altitude in the monsoon season, which was contrary to the increasing BC AAOD with increasing altitude[35]. Hence, the observational results from the Himalayas contradict the concept that SSA is mainly regulated by aerosol absorption in the Himalayas and South Asia. Inadequate understanding of SSA might cause substantial uncertainties for estimating aerosol radiative effects in climate models. Therefore, it is crucial to reveal the primary modulating factor of SSA in the Himalayas, which may also exert important implications for understanding aerosol radiative effects in South Asia as well as globally.

RESULTS AND DISCUSSION

Low SSA revealed by in situ observations over two Himalayan sites

Extremely low aerosol loading was observed over the two selected Himalayan sites during the field campaigns (Fig. 1 and Supplementary Table 1). The average scattering coefficients at 550 nm were 3.81 ± 3.84 and $4.59 \pm 2.28\ Mm^{-1}$ over Yadong and Qomolangma (Mt. Everest) Station for Atmospheric and Environmental Observation and Research(QOMS), respectively. The average absorption coefficients at 520 nm were 1.77 ± 1.35 and

[1]Key Laboratory for Semi-Arid Climate Change of the Ministry of Education, College of Atmospheric Sciences, Lanzhou University, Lanzhou 730000, China. [2]Collaborative Innovation Center for Western Ecological Safety, Lanzhou University, Lanzhou 730000, China. ✉email: hjp@lzu.edu.cn; zhanglei@lzu.edu.cn

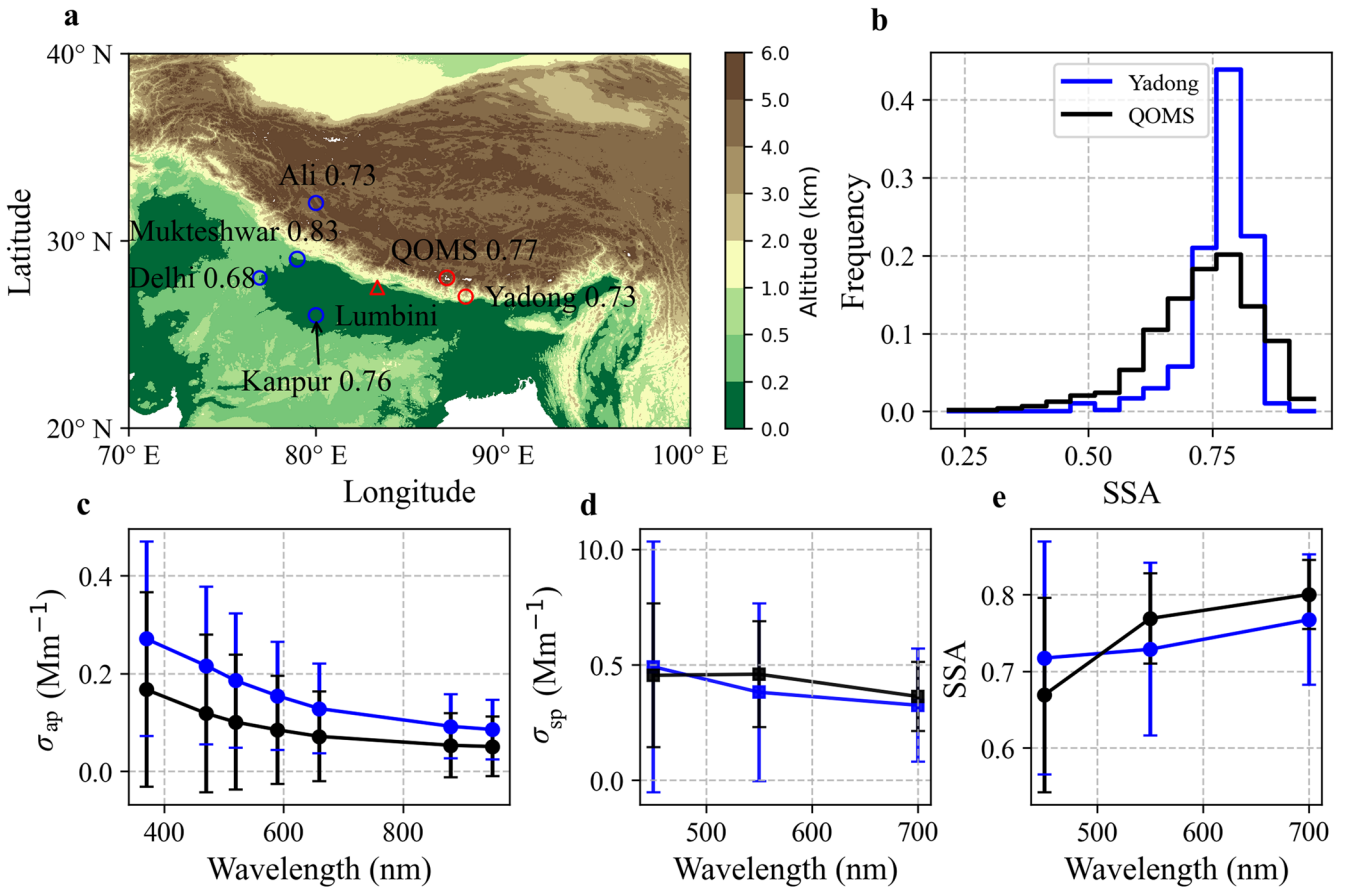

Fig. 1 Aerosol scattering and absorption coefficients and SSA over the Himalayas. Map of in situ observation sites of Yadong and QOMS and the AERONET site of Lumbini in the present study; Bangalore, India[24]; Kanpur, India[25]; Delhi, India[23]; Mukteshwar, India[27]; and Ali, China[36] (**a**). In situ observed SSAs over these sites are also shown on the map. Frequency distribution of SSA at 550 nm over Yadong and QOMS (**b**). Wavelength dependence of the absorption coefficient (**c**), scattering coefficient (**d**), and SSA (**e**) over Yadong and QOMS. Topography information is provided by ETOPO2 Global Relief Model website (https://www.ngdc.noaa.gov/mgg/global/) of National Oceanic and Atmospheric Administration. Error bars represent the standard deviations.

$1.39 \pm 0.30\ Mm^{-1}$ over Yadong and QOMS, respectively. Surprisingly, SSAs as low as 0.73 ± 0.11 and 0.77 ± 0.06 at 550 nm were obtained over Yadong and QOMS, respectively.

The absorption coefficients were apparently higher over Yadong than over QOMS at the seven wavelengths, while the scattering coefficients over the two sites seemed to be more complicated at three wavelengths (Fig. 1c, d and Supplementary Table 1). The absorption Ångström exponent (AAE) over Yadong and QOMS were 1.18 ± 0.24 and 1.35 ± 0.22, respectively. The scattering coefficients over Yadong decreased from 450 to 700 nm, whereas those over QOMS slightly increased from 450 to 550 nm and then decreased from 550 to 700 nm. Hence, SSA over Yadong slightly increased with increasing wavelength, whereas SSA over QOMS increased faster from 450 to 550 nm but slower from 550 to 700 nm (Fig. 1e).

Low ambient SSA values in the solar wavelength range between 0.60 and 0.85 have been recorded over urban sites in South Asia as well as in the Himalayas[23–27]. A recent study also recorded a low SSA of 0.73 at 870 nm using in situ observations of a photoacoustic extinctiometer over a western Tibetan Plateau site[36]. Such a low SSA over the Himalayas is expected to cause high radiative forcing efficiencies[37]. BC from the South Asian could be transported more efficiently than the other aerosols to the Himalayas given its lower scavenging efficiency[38]. Hence, strong aerosol absorption caused by a high fraction of BC and aerosol aging was suggested to be the reason for the low SSA values in South Asia and Himalayan regions in previous studies[35]. However, the wavelength dependence of the SSA seemed to be better related to that of the scattering coefficient than to that of the absorption coefficient (Fig. 1c–e). The increasing SSA wavelength dependence in the present study was similar to those for organic matter and mineral dust aerosols but opposite to that of BC-dominated aerosols[39,40]. Thus, the following sections will examine the primary regulating factor of SSA and the consequent impacts on radiative effects.

Aerosol size distribution modulates scattering efficiency and SSA

To reveal the primary determining factor of SSA over the Himalayas, the relationships between SSA and aerosol parameters, such as the absorption coefficient (σ_{ap}), the scattering coefficient (σ_{sp}), the scattering Ångström exponent (SAE), AAE, and fine and coarse aerosol sizes, were studied using in situ observations at Yadong (Fig. 2). It is unexpected that SSA exhibited a weak correlation with σ_{ap} (the Pearson correlation coefficient (r) = −0.04, the Spearman's rank correlation coefficient (ρ) = 0.08) but a significant positive correlation with σ_{sp} ($r = 0.54$, $\rho = 0.65$) (Fig. 2a, b). The negative correlation for SSA and the absorption can be clearly seen only after choosing the different levels of scatterings to make the plots. However, the positive correlation for SSA and the scattering is clearly shown for both total samples and after choosing the different levels of absorptions to make the plots. This finding is in contrast with results for urban environments where SSA is negatively correlated with absorption but

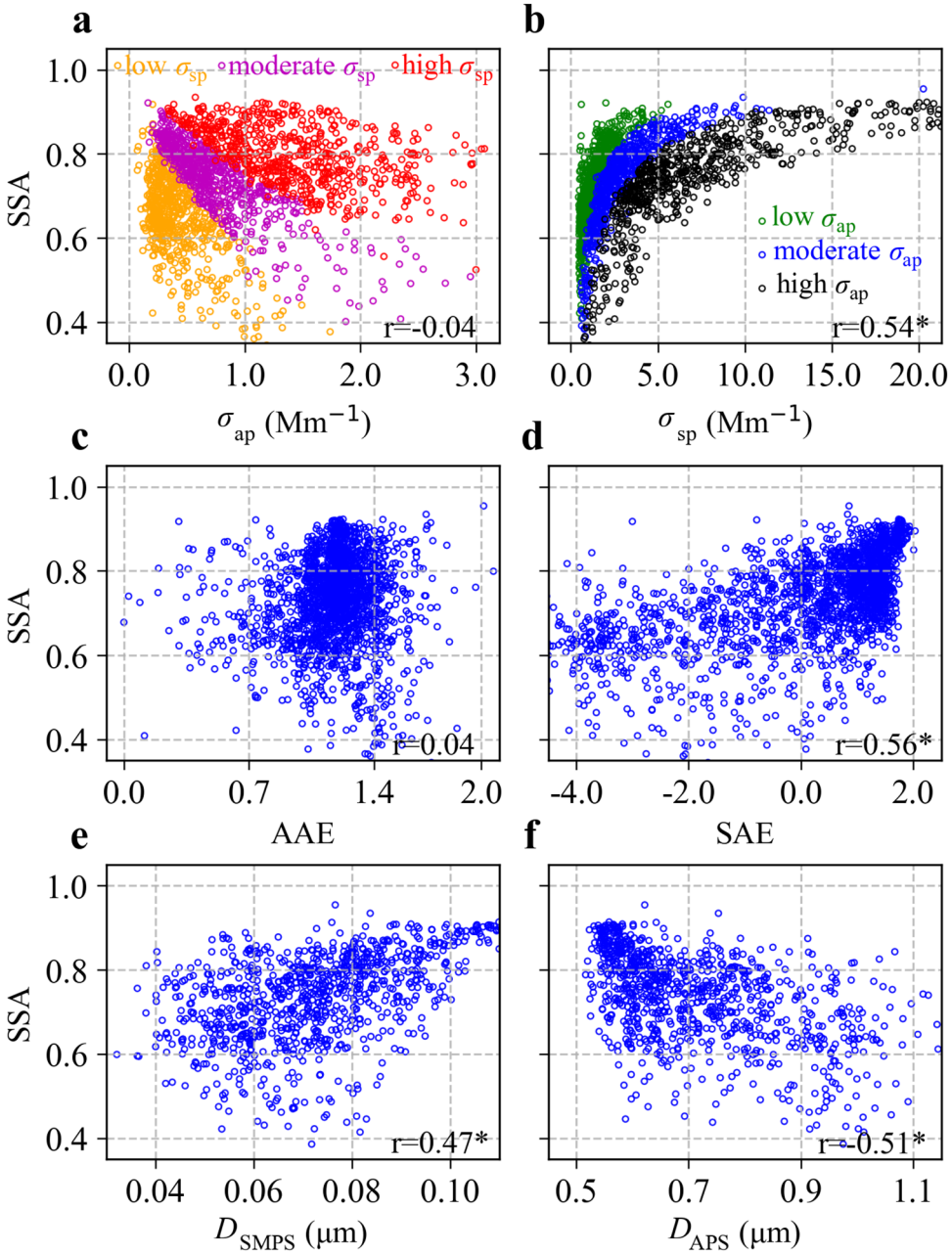

Fig. 2 The relationships between the aerosol parameters and SSA. Relationships between SSA at 550 nm and aerosol parameters, σ_{ap} at 520 nm (**a**), σ_{sp} at 550 nm (**b**), AAE calculated via power-law fitting using absorption coefficients at 370, 470, 520, 590, 660, 880, and 950 nm wavelengths (**c**), SAE derived from the scattering coefficients at 450 and 700 nm wavelengths (**d**), and fine and coarse aerosol sizes (**e**, **f**), over Yadong. D_{SMPS} and D_{APS} represent the mean diameter of fine-mode aerosols derived from scanning mobility particle sizer (SMPS) observations and coarse-mode aerosols derived from aerodynamic particle sizer spectrometer (APS) observations, respectively. The correlation coefficient between SSA and the aerosol parameter are shown in each subplot and an asterisk indicates that the correlation is significant at the significance level of 0.05.

positively dependent on scattering coefficients[22,41]. The multi-linear regression with standardized data was applied to robustly quantify the relative importance of changes in scattering and absorption on the variation of SSA. The regression result using standardized SSA ($\widehat{SSA}$), scattering coefficient ($\hat{\sigma}_{sp}$), and absorption ($\hat{\sigma}_{ap}$) is as follows:

$$\widehat{SSA} = 1.01\hat{\sigma}_{sp} - 0.71\,\hat{\sigma}_{ap} \quad (1)$$

The noticeably higher absolute value of the regression coefficient of $\hat{\sigma}_{sp}$ than that of $\hat{\sigma}_{ap}$ robustly indicated that SSA was better correlated with scattering than with absorption. This is further validated by the sensitivity analysis using SALib (Supplementary Table 2), with both first and total-order indices for the scattering were significantly higher than those for the absorption.

A weak correlation was observed between SSA and AAE (Fig. 2c), indicating that SSA was not related to absorbing aerosol species. A significant positive correlation was found between SSA and SAE (Fig. 2d), indicating the potential influence of aerosol size on SSA. Specifically, SSA exhibited a significant positive correlation with fine-mode aerosol size and a significant negative correlation with coarse-mode aerosol size (Fig. 2e, f), implying that smaller

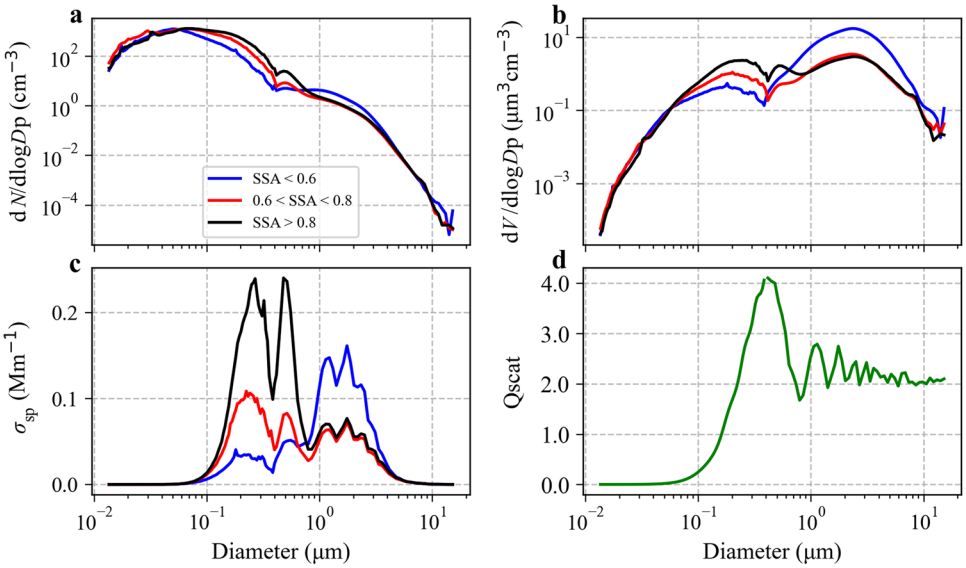

Fig. 3 The aerosol size distribution determines the scattering coefficient and thus modulates SSA. The number (**a**) and volume (**b**) size distributions, scattering coefficient (**c**) and efficiency (**d**) as a function of aerosol size at different SSA levels derived from observations at Yadong and Mie codes.

fine-mode and larger coarse-mode aerosols contributed to lower SSA. The positive correlation between SSA and SAE was opposite to the negative correlation recorded in the sub-Arctic area, where a lower SSA was found for smaller absorbing aerosols[42]. Studies have revealed that coarse-mode dust aerosols tend to have a lower SSA[43–45]. Other studies have suggested that rapid secondary aerosol formation may increase the SSA in urban pollution[46–49], which is probably related to the fine-mode size distribution. In summary, smaller fine-mode and larger coarse-mode aerosols contributed to lower SSA over Yadong. Observations over the QOMS showed similar results (Supplementary Fig. 3).

The aerosol number and volume size distributions at various SSA levels were studied to better investigate the effect of size distribution on scattering and thus on SSA (Fig. 3). The nucleation and Aitken-mode aerosols had minimal impact on scattering. The accumulation-mode aerosols were clearly separated by different SSA levels both in number and volume size distributions (Fig. 3a, b). The peak sizes of the accumulation-mode aerosols at different SSA levels increased with increasing SSA. Thus, fewer accumulation-mode aerosols were related to lower SSA, whereas the lowest SSA corresponded to the highest coarse-mode aerosols. The aerosol size distribution combined with the spectral scattering efficiency provided a reasonable explanation for the significant positive correlation between SSA and the scattering coefficient: (1) the accumulation-mode aerosols were in the size range where scattering efficiency increased monotonically with increasing wavelength; (2) the peak sizes of the accumulation-mode aerosols corresponded to high scattering efficiencies; and (3) the accumulation-mode aerosol loadings were positively correlated to their peak sizes (Fig. 3c, d). The coarse-mode aerosols exhibited a lower scattering efficiency than that of the accumulation-mode aerosols. The scattering efficiency generally decreased with increasing wavelength in the size range of coarse-mode aerosols. As a result, the coarse-mode aerosols at the SSA < 0.60 level corresponded to the highest aerosol loading. To conclude, fewer and smaller accumulation modes combined with more and larger coarse-mode aerosols resulted in lower SSA; SSA was mainly modulated by accumulation-mode aerosols rather than coarse-mode aerosols.

A positive correlation between the aerosol SSA and the Ångström exponent has also been observed in observations conducted in South Asia and has been attributed to large absorbing particles, such as dust aerosols[34]. The findings in the present study indicate that aerosol size distribution rather than absorption might be the main cause for the positive correlation between aerosol SSA and the Ångström exponent. A study based on AERONET data suggested that a higher BC concentration leads to a lower SSA at elevated locations in the Himalayas[35]. However, the fine volume fraction decreased while the linear depolarization ratio increased with increasing altitude in the monsoon season[35], which seemed to be opposite to the increasing BC concentration with altitude and indicated the influence of aerosol size distribution on SSA. In summary, the observational results contradict the concept that SSA is mainly regulated by aerosol absorption in the Himalayas and South Asia. The present study revealed that the primary modulating factor of SSA in the Himalayas was size distribution rather than absorption. These new findings may help reduce radiative forcing uncertainties in climate models and have important implications for understanding aerosol radiative effects in South Asia as well as globally.

Impacts of aerosol size distribution on radiative forcing in the Himalayas

The AERONET data from a Himalayan site in Lumbini were used to study the impacts of aerosol size distribution on radiative forcing in the Himalayas. The impacts of aerosol size distribution on SSA were clearly reflected in the AERONET data (Fig. 4), although the columnar AERONET data are different from the in situ surface observations (Sections “Field campaigns and data processing” and “AERONET data and aerosol radiative forcing efficiency”). The columnar SSA was also suggested to be greater than that derived from the in situ surface observations[50–52], partially due to the vertical variation in aerosol scattering and absorption[53]. The fine-mode aerosol sizes were clearly distinguished by different SSA levels: larger fine-mode sizes corresponded to higher SSA (Fig. 4a). Aerosol samples with the highest SSA also exhibited the fewest coarse-mode aerosols, whereas the other samples exhibited comparable coarse-mode aerosols. Furthermore, SSA was significantly positively correlated with fine-mode aerosol size and negatively correlated with coarse-mode aerosol size (Fig. 4b, c, and Supplementary Fig. 4). Such impacts of aerosol size distribution on SSA were, to some extent, similar to the results derived from in situ observations at Yadong.

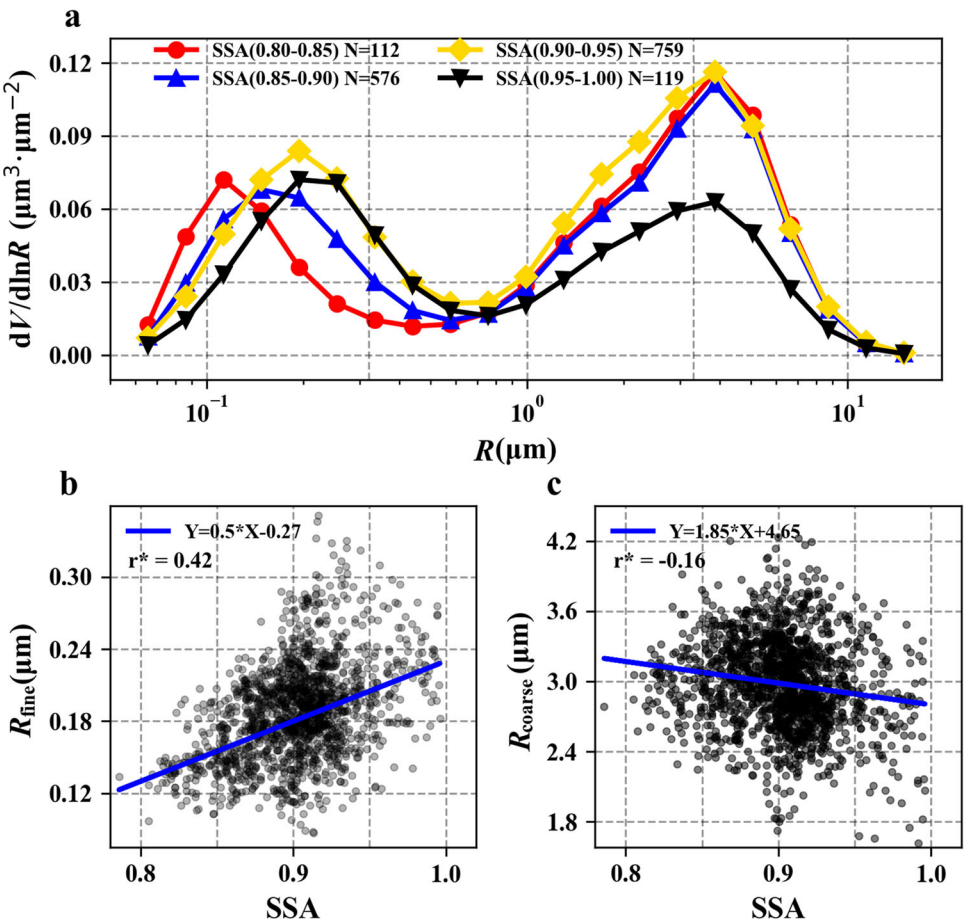

Fig. 4 The relationships between aerosol size distribution and SSA derived from AERONET data. Aerosol volume size distribution at different SSA levels (**a**), scatter plots of SSA and fine-mode aerosol size (**b**), and scatter plots of SSA and coarse-mode aerosol size (**c**) from AERONET data at the Lumbini site. R_{fine} and R_{coarse} represent the median volume radii of fine and coarse-mode aerosols, respectively. The wavelength for SSA was 550 nm. An asterisk indicates that the correlation is significant at the significance level of 0.05.

The impact of SSA on the aerosol direct radiative forcing (ADRF) in the Himalayas was further analyzed (Fig. 5). The ADRF was strongly dependent on both the AAOD and scattering aerosol optical depth (SAOD) at the bottom of the atmosphere (BOA), indicating that the cooling effect of aerosols increased with increasing absorption and scattering (Fig. 5c and Supplementary Fig. 5). As SSA is positively correlated with scattering and negatively correlated with absorption, ADRF exhibited a weaker correlation with SSA compared with its correlations with AAOD and SAOD at the BOA. Nevertheless, the ADRF decreased with decreasing SSA, indicating that a lower SSA led to higher BOA cooling. An intensive parameter, aerosol radiative forcing efficiency (ARFE), was defined to better show the impact of SSA on ADRF. ARFE was less dependent on SAOD and AAOD at the BOA when compared with the correlations of ADRF with SAOD and AAOD (Fig. 5f and Supplementary Fig. 5). ARFE became strongly positively dependent on SSA, that is, a lower SSA corresponded to a higher BOA cooling efficiency.

At TOA, ADRF exhibited a strong negative correlation with SAOD, a weak negative correlation with AAOD, and a medium negative correlation with SSA (Fig. 5a and Supplementary Fig. 6). However, ARFE exhibited a medium negative correlation with SAOD, a strong positive correlation with AAOD, and a medium negative correlation with SSA. Thus, the TOA cooling effect increased with increasing AAOD and SAOD, but the TOA cooling efficiency decreased with increasing AAOD and SAOD. Furthermore, a lower SSA corresponded to a lower TOA cooling efficiency.

In the atmosphere (ATM), ADRF exhibited a strong positive correlation with both AAOD and SAOD (Fig. 5b and Supplementary Fig. 7), indicating the importance of both aerosol absorption and scattering in heating the atmosphere. A medium negative correlation was found between ADRF and SSA. However, ARFE exhibited a weak negative correlation with SAOD and a weak positive correlation with AAOD but a strong negative correlation with SSA (Fig. 5e and Supplementary Fig. 7), which further confirmed that SSA considerably impacts aerosol radiative effects in addition to aerosol loading.

Two important results can be summarized from the relationships among SSA, AAOD, SAOD, ADRF, and ARFE: (1) the absolute values of the correlation coefficients of ARFE and SSA were higher than those of ADRF and SSA at BOA, TOA, and ATM; (2) the sign of the AAOD-AREF correlation may be opposite to that of the AAOD-ADRF correlation, as well as for the SAOD-AREF and SAOD-ADRF correlations, but the SSA-AREF and SSA-ADRF correlations exhibited the same signs at BOA, TOA, and ATM. In summary, SSA significantly impacts AREF: a lower SSA may cause more BOA cooling, less TOA cooling, and more ATM heating with the same aerosol loading.

The crucial impacts of aerosol size distribution on SSA were clearly portrayed using in situ observations, and the influence of SSA on radiative effects was further revealed based on AERONET data in this study. These findings contradict previous research suggesting that SSA is primarily governed by absorption from large amounts of BC, absorption enhancement from aerosol aging,

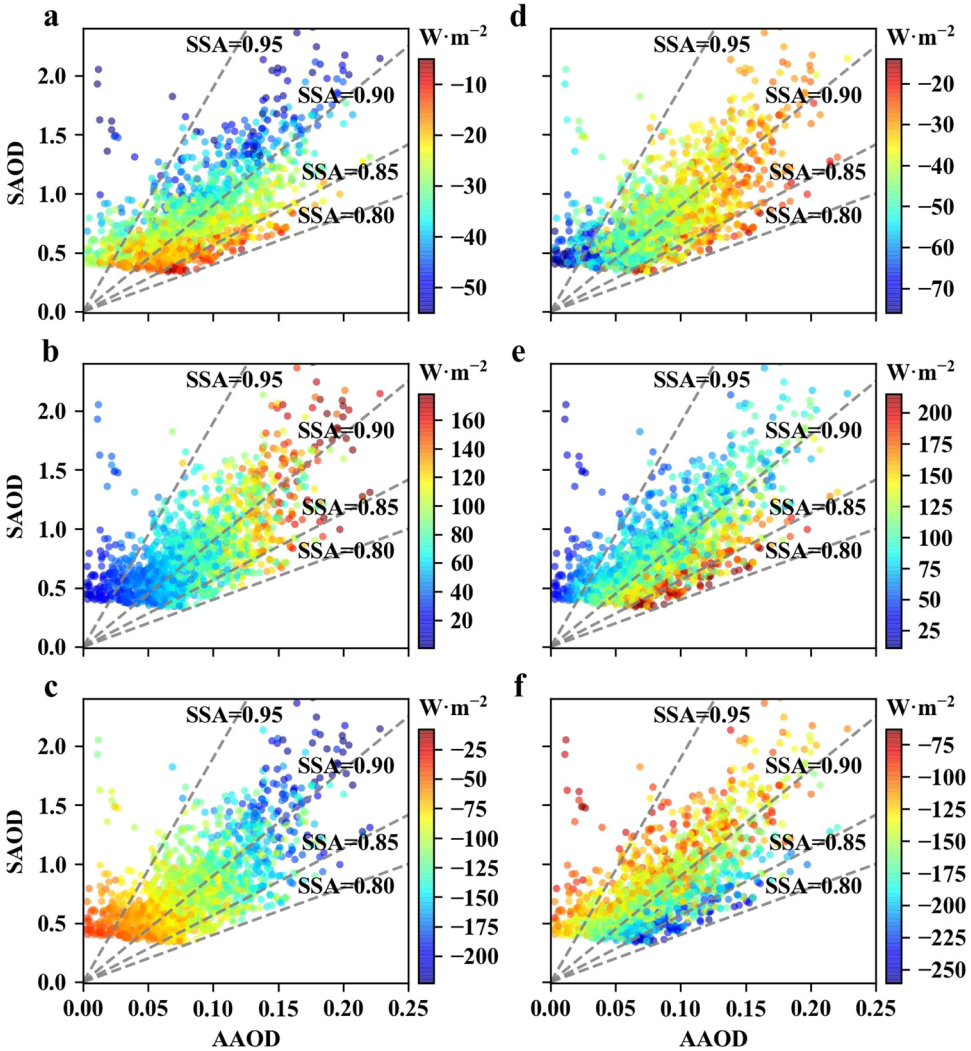

Fig. 5 The effect of SSA on radiative forcing. ADRF (**a**–**c**) and ARFE (**d**–**f**) as a function of AAOD and SAOD at the top of the atmosphere (TOA) (**a**, **d**), in the atmosphere (**b**, **e**), and at the BOA (**c**, **f**) at the AERONET site in Lumbini. The dashed lines represent the SSA contours. The wavelength for AAOD and SAOD was 550 nm.

or absorption from coarse-mode mineral dust in the Himalayas and South Asia[34,35,54]. The new findings in the present study can better explain the variation in SSA and the consequent radiative effects in the Himalayas, which may also have important insights into reducing radiative effect uncertainties in climate models and understanding aerosol radiative effects in South Asia as well as globally.

METHODS

Field campaigns and data processing

As part of the Second Tibetan Plateau Scientific Expedition and Research Program, two intensive field campaigns on atmospheric aerosols were conducted during the summer monsoon season in the Himalayas. One field campaign was conducted at Yadong (27.42°N, 88.90°E, 3136 m a.s.l.) from June 11, 2021 to August 31, 2021 (Supplementary Fig. 1) and the other one was at Qomolangma (Mt. Everest) Station for Atmospheric and Environmental Observation and Research (QOMS; 28.36°N, 86.95°E, 4276 m a.s.l.) from May 20, 2022 to June 13, 2022. The aerosol scattering and absorption coefficients and size distributions collected during the field campaigns were used in the present study.

The scattering coefficient (σ_{sp}) was measured using an integrating Nephelometer (model 3563, TSI Inc., USA), and the absorption coefficient (σ_{ap}) was derived from the observations of a seven-wavelength Aethalometer (model AE33, Magee Scientific, USA). An inlet for particles <2.5 µm was set during sampling. Nafion drying tubes were used to dry the sampling air only at Yadong, whereas the ambient air was directly sampled at QOMS for measuring scattering and absorption coefficients. The scattering coefficients at 450, 550, and 700 nm wavelengths were corrected for truncation errors using the method presented by Anderson and Ogren[55]. The SSAs at 450, 550, and 700 nm were calculated from σ_{ap} and σ_{sp}:

$$SSA = \sigma_{sp}/(\sigma_{sp} + \sigma_{ap}) \quad (2)$$

SSA has been widely used to infer aerosol absorbability in observations and numerical simulations[56]. Then, the scattering Ångström exponent (SAE) was calculated as follows:

$$SAE = -\frac{\log(\sigma_{sp,\lambda_1}) - \log(\sigma_{sp,\lambda_2})}{\log(\lambda_1) - \log(\lambda_2)} \quad (3)$$

where $\lambda_1 = 450$ and $\lambda_2 = 700$ nm. The absorption Ångström exponent (AAE) is used to express the relationship between σ_{ap} and wavelength (λ):

$$\sigma_{ap}(\lambda) = k\lambda^{-AAE} \quad (4)$$

where k is a constant. The AAE was calculated via power-law fitting using σ_{ap} at the wavelengths of 370, 470, 520, 590, 660, 880, and 950 nm.

The number size distribution of ultrafine particles with a Stokes diameter (*D*p) from 13.6 to 514 nm was measured using a scanning mobility particle sizer (SMPS; 3082, TSI Inc.). An aerodynamic particle sizer spectrometer (APS; model 3321, TSI Inc.) was also used to observe size distributions from 542 nm to 19.81 μm (aerodynamic diameter (*D*a)). For consistency, observations from the APS were converted to the Stokes diameter while assuming the particle density as 1.7 μg m^{-3} [57]. Considering the aerosol size distributions from in situ observations and AERONET in the present study, a threshold of 600 nm was applied to define the fine-mode (*D*a < 600 nm) and coarse-mode (*D*a > 600 nm) aerosols following the AERONET algorithm[58]. The fine-mode aerosols were further classified into nucleation (*D*a < 25 nm), Aitken (25 nm < *D*a < 100 nm), and accumulation (25 nm < *D*a < 600 nm) modes[59].

Scattering coefficients were also derived from the size distribution and Mie theory[60]:

$$\sigma_{sp}(m,\lambda) = \int Q_s(D_p, m, \lambda)\frac{\pi}{4}D_p^2 n(D_p)dD_p \quad (5)$$

where Q_s is the scattering efficiency calculated using the Mie code, and the refractive index m was set to 1.426[61]. The calculated aerosol scattering coefficient is consistent with the measured coefficient (Supplementary Fig. 2).

AERONET data and aerosol radiative forcing efficiency

The AERONET data at the Himalayan site of Lumbini (27.49°N, 83.28°S, 110 m a.s.l.) were used to link aerosol size distribution, SSA, and radiative forcing. The Lumbini site was selected because it is the nearest site to Yadong and QOMS with long-term data from 2013 to 2019. The level 2.0 aerosol optical depth (AOD) and inversion data, including volume size distribution, SSA, fine and coarse-mode volume median radius, and aerosol direct radiative forcing (ADRF; ΔF), were used[62]. The aerosol radiative forcing efficiency (ARFE; ΔF^{eff}) was defined to better investigate the influence of intensive parameters (e.g., SSA) on ADRF[37]:

$$\Delta F^{eff} = \Delta F / AOD_{550nm} \quad (6)$$

where $AOD_{550\ nm}$ is the AOD at 550 nm.

Standardized regression, sensitivity analysis, and correlation coefficients

To robustly judge whether absorption or scattering is more sensitive to SSA, a simple standardized regression and a comprehensive sensitivity analysis were used. Data with different dimensions or large numerical differences should be standardized before being used for multiple linear regression analysis[63]. For example, the regression equation for one dependent variable (Y) and two independent variables (X_1 and X_2) is given as follows:

$$Y = c_0 + a_0 X_1 + b_0 X_2 \quad (7)$$

where c_0 is a constant and a_0 and b_0 are the regression coefficients. The standardization of a variable X (might be Y, X_1 and X_2) is expressed as follows:

$$\hat{X}_i = (X_i - \overline{X})/\sigma_X \quad (8)$$

where $\overline{X}$ is the average and σ_X is the standard deviation of X. The regression equation of the standardized variables $\hat{Y}$, $\hat{X}_1$ and $\hat{X}_2$ is given as follows:

$$\hat{Y} = a_1 \hat{X}_1 + b_1 \hat{X}_2 \quad (9)$$

The regression coefficients a_1 and b_1 can be compared directly. This data standardization was applied for multiple linear regression analysis of SSA, σ_{ap}, and σ_{sp} in "AERONET data and aerosol radiative forcing efficiency" since there were large numerical differences between σ_{sp} and σ_{ap}.

A comprehensive sensitivity analysis using the Sensitivity Analysis Library in Python (SALib)[64] was also performed to judge the relative importance of scattering and absorption to SSA. The SALib, which provides several commonly used global sensitivity analysis methods, is useful to calculate the influence of model inputs or exogenous factors on outputs of interest[65]. The result of the SALib includes first, second, and total-order indices combined with their corresponding confidence intervals.

The Pearson correlation coefficient (r) is used to quantify the relationships between two aerosol parameters. For two parameters that exhibited nonlinear relationships such as SSA and scattering coefficient, the Spearman's rank correlation coefficient (ρ) was applied. Unless specifically stated, the Pearson correlation coefficient is generally used.

DATA AVAILABILITY

The in situ observation data at Yadong and QOMS sites is freely available on the website of the National Tibetan Plateau Data Center (http://data.tpdc.ac.cn/en/). The AERONET data is freely available on the AERNOET website (https://aeronet.gsfc.nasa.gov/).

CODE AVAILABILITY

The codes that support the findings of this study are available from the corresponding authors on request.

Received: 6 December 2022; Accepted: 3 May 2023;
Published online: 30 May 2023

REFERENCES

1. Kok, J. F. et al. Integrative analysis of desert dust size and abundance suggests less dust climate cooling. *Nat. Geosci.* **10**, 274–278 (2017).
2. Nishant, N., Sherwood, S. C. & Geoffroy, O. Aerosol-induced modification of organised convection and top-of-atmosphere radiation. *npj Clim. Atmos. Sci.* **2**, 33 (2019).
3. Liu, D., He, C., Schwarz, J. P. & Wang, X. Lifecycle of light-absorbing carbonaceous aerosols in the atmosphere. *npj Clim. Atmos. Sci.* **3**, 40 (2020).
4. Li, J. et al. Scattering and absorbing aerosols in the climate system. *Nat. Rev. Earth Environ.* **3**, 363–379 (2022).
5. Li, J. et al. Impacts ofmeteorology and vegetation on surface dust concentrations in Middle Eastern countries. *Sci. Total Environ.* **712**, 136597 (2022).
6. Russell, P. B. et al. Comparison of aerosol single scattering albedos derived by diverse techniques in two North Atlantic experiments. *J. Atmos. Sci.* **41**, 609–619 (2002).
7. Fu, Q., Thorsen, T. J., Su, J., Ge, J. M. & Huang, J. P. Test of Mie-based single-scattering properties of non-spherical dust aerosols in radiative flux calculations. *J. Quant. Spectrosc. Radiat. Transf.* **110**, 1640–1653 (2009).
8. Devi, A. & Satheesh, S. K. Global maps of aerosol single scattering albedo using combined CERES-MODIS retrieval. *Atmos. Chem. Phys.* **22**, 5365–5376 (2022).
9. Haywood, J. M. & Shine, K. P. The effect of anthropogenic sulfate and soot aerosol on the clear sky planetary radiation budget. *Geophys. Res. Lett.* **5**, 603–606 (1995).
10. Takemura, T., Nakajima, T., Dubovik, O., Holben, B. N. & Kinne, S. Single-scattering albedo and radiative forcing of various aerosol species with a global three-dimensional model. *J. Clim.* **15**, 333–352 (2002).
11. Thorsen, T. J., Ferrare, R. A., Kato, S. & Winker, D. M. Aerosol direct radiative effect sensitivity analysis. *J. Clim.* **33**, 6119–6139 (2020).
12. Jeong, J. I. et al. Parametric analysis for global single scattering albedo calculations. *Atmos. Environ.* **234**, 1352–2310 (2020).

13. Brown, H. et al. Biomass burning aerosols in most climate models are too absorbing. *Nat. Commun.* **12**, 277 (2021).
14. Zhang, L. et al. Clear-sky direct aerosol radiative forcing uncertainty associated with aerosol vertical distribution based on CMIP6 models. *J. Clim.* **35**, 3021–3035 (2022).
15. Qiu, C., Khalizov, A. F., Hogan, B., Petersen, E. L. & Zhang, R. High sensitivity of diesel soot morphological and optical properties to combustion temperature in a shock tube. *Environ. Sci. Technol.* **48**, 6444–6452 (2014).
16. China, S. et al. Morphology and mixing state of aged soot particles at a remote marine free troposphere site: Implications for optical properties. *Geophys. Res. Lett.* **42**, 1243–1250 (2015).
17. Ni, H. et al. Brown carbon in primary and aged coal combustion emission. *Environ. Sci. Technol.* **55**, 5701–5710 (2021).
18. Bond, T. C. & Bergstrom, R. W. Light absorption by carbonaceous particles: an investigative review. *Aerosol Sci. Technol.* **40**, 27–67 (2006).
19. Moosmüller, H. et al. Single scattering albedo of fine mineral dust aerosols controlled by iron concentration. *J. Geophys. Res. Atmos.* **117**, D11210 (2012).
20. Liu, S. et al. Aerosol single scattering albedo dependence on biomass combustion efficiency: laboratory and field studies. *Geophys. Res. Lett.* **41**, 742–748 (2014).
21. Li, J., Carlson, B. E. & Lacis, A. A. Using single-scattering albedo spectral curvature to characterize East Asian aerosol mixtures. *J. Geophys. Res. Atmos.* **120**, 2037–2052 (2015).
22. Tian, P. et al. Potential influence of fine aerosol chemistry on the optical properties in a semi-arid region. *Environ. Res.* **216**, 0013–9351 (2023).
23. Ganguly, D., Jayaraman, A., Rajesh, T. A. & Gadhavi, H. Wintertime aerosol properties during foggy and nonfoggy days over urban center Delhi and their implications for shortwave radiative forcing. *J. Geophys. Res.* **111**, D15217 (2006).
24. Babu, S. S., Satheesh, S. K. & Moorthy, K. K. Aerosol radiative forcing due to enhanced black carbon at an urban site in India. *Geophys. Res. Lett.* **29**, 27 (2002).
25. Tripathi, S. N. Aerosol black carbon radiative forcing at an industrial city in northern India. *Geophys. Res. Lett.* **32**, L08802 (2005).
26. Ramana, M. V., Ramanathan, V., Podgorny, I. A., Pradhan, B. B. & Shrestha, B. The direct observations of large aerosol radiative forcing in the Himalayan region. *Geophys. Res. Lett.* **31**, L05111 (2004).
27. Hooda, R. K. et al. Driving factors of aerosol properties over the foothills of Central Himalayas based on 8.5 years continuous measurements. *J. Geophys. Res. Atmos.* **123**, 13421–13442 (2018).
28. Chen, P. et al. Carbonaceous aerosol characteristics on the third pole: a primary study based on the atmospheric pollution and cryospheric change (APCC) network. *Environ. Pollut.* **253**, 49–60 (2019).
29. Yuan, Q. et al. Evidence for large amounts of brown carbonaceous tarballs in the Himalayan atmosphere. *Environ. Sci. Technol. Lett.* **8**, 16–23 (2020).
30. Pandithurai, G., Pinker, R. T., Takamura, T. & Devara, P. C. S. Aerosol radiative forcing over a tropical urban site in India. *Geophys. Res. Lett.* **31**, L12107 (2004).
31. Shamjad, P. M. et al. Contribution of brown carbon to direct radiative forcing over the Indo-Gangetic Plain. *Environ. Sci. Technol.* **49**, 10474–10481 (2015).
32. Ramachandran, S., Rupakheti, M. & Lawrence, M. G. Aerosol-induced atmospheric heating rate decreases over South and East Asia as a result of changing content and composition. *Sci. Rep.* **10**, 20091 (2020).
33. Hyvärinen, A. P. et al. Continuous measurements of optical properties of atmospheric aerosols in Mukteshwar, northern India. *J. Geophys. Res. Atmos.* **114**, D08207 (2009).
34. Goto, D., Badarinath, K. V. S., Takemura, T. & Nakajima, T. Simulation of aerosol optical properties over a tropical urban site in India using a global model and its comparison with ground measurements. *Ann. Geophys.* **29**, 955–963 (2011).
35. Ramachandran, S., Rupakheti, M. & Lawrence, M. G. Black carbon dominates the aerosol absorption over the Indo-Gangetic Plain and the Himalayan foothills. *Environ. Int.* **142**, 105814 (2020b).
36. Zhang, L. et al. Unexpected high absorption of atmospheric aerosols over a western Tibetan Plateau Site in summer. *J. Geophys. Res. Atmos.* **126**, 033286 (2021).
37. Tian, P. et al. Radiative absorption enhancement of dust mixed with anthropogenic pollution over East Asia. *Atmos. Chem. Phys.* **18**, 7815–7825 (2018).
38. Liu, D. et al. Efficient vertical transport of black carbon in the planetary boundary layer. *Geophys. Res. Lett.* **47**, e2020GL088858 (2020).
39. Samset, B. H. et al. Aerosol absorption: progress towards global and regional constraints. *Curr. Clim. Change Rep.* **4**, 65–83 (2018).
40. Di Biagio, C. et al. Complex refractive indices and single-scattering albedo of global dust aerosols in the shortwave spectrum and relationship to size and iron content. *Atmos. Chem. Phys.* **19**, 15503–15531 (2019).
41. Chang, Y. et al. Changes in physical and chemical properties of urban atmospheric aerosols and ozone during the COVID-19 lockdown in a semi-arid region. *Atmos. Environ.* **287**, 119270 (2022).
42. Mogo, S. et al. In situ measurements of aerosol optical properties and number size distributions in a coastal region of Norway during the summer of 2008. *Atmos. Chem. Phys.* **12**, 5841–5857 (2012).
43. Ryder, C. L. et al. Optical properties of Saharan dust aerosol and contribution from the coarse mode as measured during the Fennec 2011 aircraft campaign. *Atmos. Chem. Phys.* **13**, 303–325 (2013).
44. Khatri, P., Takamura, T., Shimizu, A. & Sugimoto, N. Observation of low single scattering albedo of aerosols in the downwind of the East Asian desert and urban areas during the inflow of dust aerosols. *J. Geophys. Res. Atmos.* **119**, 787–802 (2014).
45. Saito, M. & Yang, P. Advanced bulk optical models linking the backscattering and microphysical properties of mineral dust aerosol. *Geophys. Res. Lett.* **48**, 095121 (2021).
46. Cheng, Y. F. et al. Influence of soot mixing state on aerosol light absorption and single scattering albedo during air mass aging at a polluted regional site in northeastern China. *J. Geophys. Res.* **114**, 010883 (2009).
47. Han, T. et al. Aerosol optical properties measurements by a CAPS single scattering albedo monitor: comparisons between summer and winter in Beijing, China. *J. Geophys. Res. Atmos.* **122**, 2513–2526 (2017).
48. Wang, W. et al. Exploring the drivers and photochemical impact of the positive correlation between single scattering albedo and aerosol optical depth in the troposphere. *Environ. Sci. Technol. Lett.* **8**, 504–510 (2021).
49. Yao, L. et al. Co-benefits of reducing PM2.5 and improving visibility by COVID-19 lockdown in Wuhan. *npj Clim. Atmos. Sci.* **4**, 40 (2021).
50. Ge, J. M., Huang, J. P., Su, J., Bi, J. R. & Fu, Q. Shortwave radiative closure experiment and direct forcing of dust aerosol over northwestern China. *Geophys. Res. Lett.* **38**, L24803 (2011).
51. Srivastava, R., Ramachandran, S., Rajesh, T. A. & Kedia, S. Aerosol radiative forcing deduced from observations and models over an urban location and sensitivity to single scattering albedo. *Atmos. Environ.* **45**, 6163–6171 (2011).
52. Andrews, E., Ogren, J. A., Kinne, S. & Samset, B. Comparison of AOD, AAOD and column single scattering albedo from AERONET retrievals and in situ profiling measurements. *Atmos. Chem. Phys.* **17**, 6041–6072 (2017).
53. Guan, X. et al. Wintertime vertical distribution of black carbon and single scattering albedo in a semi-arid region derived from tethered balloon observations. *Sci. Total Environ.* **807**, 150790 (2022).
54. Ganguly, D., Gadhavi, H., Jayaraman, A., Rajesh, T. A. & Misra, A. Single scattering albedo of aerosols over the central India: Implications for the regional aerosol radiative forcing. *Geophys. Res. Lett.* **32**, L18803 (2005).
55. Anderson, T. L. & Ogren, J. A. Determining aerosol radiative properties using the TSI 3563 integrating nephelometer. *Aerosol Sci. Technol.* **29**, 57–69 (1998).
56. Che, H. et al. Spatial distribution of aerosol microphysical and optical properties and direct radiative effect from the China Aerosol Remote Sensing Network. *Atmos. Chem. Phys.* **19**, 11843–11864 (2019).
57. Shang, D. et al. Particle number size distribution and new particle formation under the influence of biomass burning at a high altitude background site at Mt. Yulong (3410 m), China. *Atmos. Chem. Phys.* **18**, 15687–15703 (2018).
58. Sinyuk et al. The AERONET Version 3 aerosol retrieval algorithm, associated uncertainties and comparisons to Version 2. *Atmos. Meas. Tech.* **13**, 3375–3411 (2020).
59. Zhao et al. Response of particle number concentrations to the clean air action plan: lessons from the first long-term aerosol measurements in a typical urban valley in western China. *Atmos. Chem. Phys.* **21**, 14959–14981 (2021).
60. Bohren, C. & Huffman, D. Absorption and scattering of light by small particles. *Opt. Eng.* **23**, SR48–SR48 (1983).
61. Virkkula, A. et al. Aerosol optical properties calculated from size distributions, filter samples and absorption photometer data at Dome C, Antarctica, and their relationships with seasonal cycles of sources. *Atmos. Chem. Phys.* **22**, 5033–5069 (2022).
62. Holben, B. N. et al. AERONET - A federated instrument network and data archive for aerosol characterization. *Rem. Sens. Environ.* **66**, 1–16 (1998).
63. Asuero et al. The correlation coefficient: an overview. *Crit. Rev. Anal. Chem.* **36**, 41–59 (2006).
64. Herman, J. & Usher, W. SALib: an open-source Python library for sensitivity analysis. *J. Open Source Softw.* **2**, 97 (2017).
65. Smith, C. et al. Current fossil fuel infrastructure does not yet commit us to 1.5 °C warming. *Nat. Commun.* **10**, 101 (2019).

ACKNOWLEDGEMENTS

This research was supported by the Second Tibetan Plateau Scientific Expedition and Research Program (STEP), Grant No. 2019QZKK0602. Pengfei Tian acknowledges the National Natural Science Foundation of China (42175093 and 41905017). Jinsen Shi was also supported by the Fundamental Research Funds for the Central Universities (lzujbky-2022-kb10) and Natural Science Foundation of Gansu Province

(22JR5RA441). We thank Brent Holben, the AERONET PI at the Lumbini site, for the effort in establishing and maintaining the site.

AUTHOR CONTRIBUTIONS

J.H., L.Z., and P.T. designed the study and received the funding. P.T., Z.Y., and C.C. analyzed the data and led the writing. Z.Y., C.K., J.S., J.H., and P.T. conducted the field campaigns. All authors contributed to discussion, review, and editing.

COMPETING INTERESTS

The authors declare no competing interests.

ADDITIONAL INFORMATION

Supplementary information The online version contains supplementary material available at https://doi.org/10.1038/s41612-023-00368-5.

Correspondence and requests for materials should be addressed to Jianping Huang or Lei Zhang.

Reprints and permission information is available at http://www.nature.com/reprints

Publisher's note Springer Nature remains neutral with regard to jurisdictional claims in published maps and institutional affiliations.

Open Access This article is licensed under a Creative Commons Attribution 4.0 International License, which permits use, sharing, adaptation, distribution and reproduction in any medium or format, as long as you give appropriate credit to the original author(s) and the source, provide a link to the Creative Commons license, and indicate if changes were made. The images or other third party material in this article are included in the article's Creative Commons license, unless indicated otherwise in a credit line to the material. If material is not included in the article's Creative Commons license and your intended use is not permitted by statutory regulation or exceeds the permitted use, you will need to obtain permission directly from the copyright holder. To view a copy of this license, visit http://creativecommons.org/licenses/by/4.0/.

© The Author(s) 2023